Advances in continuously profiling the thermodynamic state of the boundary layer: Integration of measurements and methods

ULRICH LÖHNERT*, S. CREWELL*, O. KRASNOV**, E. O'CONNOR***, H. RUSSCHENBERG**

*Institute for Meteorology and Geophysics, University of Cologne, GER

** Delft University of Technology, NL

***University of Reading, UK

Manuscript version May, 2007

Submitted to *Journal of Atmospheric and Oceanic Technology – Special Issue ISTP 2006*

Corresponding Author Address:

Dr. Ulrich Löhnert

Institute for Meteorology and Geophysics

Zülpicher Straße 49a

50674 Köln

Germany

Tel: +49 +221 470 1779

Fax: +49 +221 470 5161

Email: loehnert@meteo.uni-koeln.de

Abstract

This paper describes advances in ground based thermodynamic profiling of the lower troposphere through sensor synergy. The well documented Integrated Profiling Technique (IPT), which uses a microwave profiler, a cloud radar and a ceilometer to simultaneously retrieve vertical profiles of temperature, humidity and liquid water content of non-precipitating clouds, is further developed towards an enhanced performance in the boundary layer and lower troposphere. For a more accurate temperature profile, this is accomplished by including an elevation scanning measurement modus of the microwave profiler. Height dependent RMS accuracies of temperature (humidity) ranging from ~0.3 to 0.9 K (0.5 to 0.8 gm^{-3}) in the boundary layer are derived from retrieval simulations and confirmed experimentally with measurements at distinct heights taken during the LAUNCH 2005 campaign at the experimental site Lindenberg of the German Weather Service. Temperature inversions, especially of the lower boundary layer, are captured in a very satisfactory way by using the elevation scanning mode. In order to improve the quality of liquid water content measurements in clouds we incorporate a sophisticated target classification scheme developed within the European cloud observing network Cloudnet. It allows the detailed discrimination between different types of backscatterers detected by cloud radar and ceilometer. Finally, to allow IPT application also to drizzling cases, we integrate an LWC profiling method. This technique classifies the detected hydrometeors into three different size classes using certain thresholds determined by radar reflectivity and/or ceilometer extinction profiles. By inclusion into IPT, the retrieved profiles are made consistent with the measurements of the microwave profiler and a LWC a priori profile. Results of IPT application to 13 days of the LAUNCH campaign are analysed and the importance of integrated profiling for model evaluation is underlined.

1. Introduction

Continuous profiling of the thermodynamic state of the atmosphere is becoming more and more important in support of meso-scale models which are increasingly employed for Numerical Weather Prediction (NWP). Especially the development of the boundary layer (BL), e.g. its diurnal cycle or its influence on the initiation of convection, is crucial for the correct prediction of regional weather scales, including severe events such as extreme precipitation. In this context the operational radiosonde network with its typically 12-hourly observations is by far not sufficient for evaluating model performance on small time (short-term 0-+18 h) and spatial (model resolution < 3 km) scale. Because also satellites instruments are not able to resolve BL variables well, strong efforts have been undertaken within the last decade to enhance the development of ground-based remote sensing instrumentation. However, no single instrument is capable to observe all relevant atmospheric variables needed to investigate BL processes in detail. These are extremely relevant for assessing the performance of NWP models, as well as for investigating the potential for data assimilation of such observations. Therefore we describe an instrument combination method which is capable of continuously profiling the lower troposphere with special emphasis on an accurate boundary layer description.

The technique described here is an advancement of the Integrated Profiling Technique (IPT) described and assessed by Löhnert et al. 2004 (L04), respectively Löhnert et al. 2007 (L07). It combines measurements of a microwave profiler, a cloud radar and a ceilometer with suited a priori information to determine profiles of temperature (T), water vapor density (ρ_v) and cloud liquid water content (LWC) in a *physically consistent way*. This means that the retrieved profiles in state space can be transformed back into measurement space to match the original measurements within the assumed range of error. The major improvements compared to L04 which will be presented in this paper are the following:

1.) Instead of using only zenith observations from the Microwave Profiler (MWP), we now additionally include elevation scanning measurements which can increase the accuracy of the temperature profile significantly in the BL (Crewell and Löhnert 2007).

2.) We now employ the well established Cloudnet target classification scheme (Hogan and O'Connor 2006) developed at the University of Reading. This scheme allows for the discrimination between different hydrometeor categories, aerosols and insects when profiling the atmosphere with a ceilometer and a cloud radar. It is of essential value when applying a physically consistent method.

3.) In order to enable the applicability of the IPT to drizzling cases, we incorporate the LWC profiling method according to Krasnov and Russchenberg (2006, K06) into the IPT. This is a stand-alone method to determine the LWC profile in non-drizzling to heavy-drizzling clouds using cloud radar and ceilometer measurements. By incorporating it into the IPT, we expand the IPT applicability from non-precipitating to drizzling clouds. Through incorporation into IPT, the results of K06 are made physically consistent with the rest of the measurements.

The paper is organized as follows: In section 2 we describe the experimental setup of instruments used for this study during the LAUNCH campaign. Section 3 describes the improved IPT, with special emphasis on the target classification, the inclusion of the elevation scanning measurements of the MWP and the incorporation of the K06 retrieval algorithm. We then show results of IPT application to simulated measurements in Section 4, making clear the potential of elevation scanning measurements for BL-profiling. Section 5 shows experimental results obtained from comparisons with in situ radiosonde and mast measurements. We also emphasize the importance of continuous measurements of thermodynamic profiles by showing first comparisons with the operational NWP model "Lokal-Modell" (LME) of the German Weather Service (DWD).

2. Experimental Measurement Setup

The measurements used in this study were all part of the LAUNCH (International **L**indenberg campaign for **A**ssessment of H**U**midity a**N**d **C**loud Profiling Systems and its Impact on **H**igh-Resolution Modelling) 2005 campaign at and around the Richard-Aßmann Observatory of DWD at Lindenberg, Germany (52.17° N, 14.12° E). This campaign was chosen because here, a MWP with an elevation scanning capability of high accuracy was operated simultaneously with a cloud radar and a ceilometer. These measurements were carried out at the DWD boundary layer measurement site Falkenberg about 4 km south of Lindenberg. The area around Lindenberg and Falkenberg is dominated by farmland and varies between 50 and 120 m altitude above sea level. Additionally at the Lindenberg site, four times a day (0000, 0600, 1200 and 1800 UTC) operationally launched Vaisala RS-92 radiosondes are used as a priori information and for accuracy assessment.

2.1. Microwave Profiler

The central instrument of the applied Integrated Profiling Technique (IPT) is the 14 channel **H**umidity **A**nd **T**emperature microwave **PRO**filer (HATPRO, Rose et al. (2005), *www.radiometer-physics.de*) that was designed as a network-suitable low-cost microwave radiometer which can observe liquid water path (LWP), humidity and temperature profiles with high (1s) temporal resolution. HATPRO comprises total-power radiometers utilizing direct detection receivers within two bands. Band A contains seven channels from 22.335 to 31.4 GHz and Band B contains seven channels from 51 to 58 GHz. The channels of Band A are not only suited for determining LWP, but also contain limited information about the vertical profile of humidity through the pressure broadening of the optically thin 22.235 GHz H_2O line. The channels of Band B, on the other hand, contain information on the vertical profile of temperature. At the opaque centre of the O_2 absorption complex most of the information originates from near the surface, whereas further away from the line, the atmosphere becomes less and less opaque so that more and more information also originates from higher atmospheric layers.

In addition to the spectral information, angular information can enhance the accuracy of the temperature profile in the boundary layer. Therefore one channel systems operating around 60 GHz have been developed (Kadygrov and Pick (1998)) that derive profile information from elevation scanning. Due to the fact that the atmosphere is optically thick around 60 GHz, the observed radiation systematically originates from higher altitudes the higher the elevation angle. This information gain can be used for profile retrieval if one assumes horizontal homogeneity. Since these brightness temperatures vary only slightly with elevation angle, the method requires a highly sensitive radiometer which is typically realized by using wide bandwidths up to 4 GHz. For the HATPRO radiometer, Crewell and Löhnert (2007) have shown on the basis of statistical algorithms that, considering Band B, the combination of *spectral and angular* information shows best performance *throughout the lower troposphere* when the four most opaque frequencies are used with their angular information and the three more transparent channels are added with their zenith measurement only. Note no significant accuracy improvement is achieved for the retrieval of humidity profiles by adding elevation scanning in Band A from ground based MWP.

Microwave radiometer observations during LAUNCH were taken at Falkenberg starting on, 0900 UTC 8 September 2005 and ended on 0700 UTC 1 November 2005. Unfortunately, on 1800 UTC 17 September 2005 the GPS clock failed which led to an omission of relative calibrations until this was corrected for on 1200 UTC 17 October 2005. Because the data in this time interval are of poor quality they are ignored in the following. HATPRO was operated in a dual zenith/elevation-scanning mode: The elevation scans were carried out every

20 min and lasted about 5 min each with an integration time of 30 s at each angle. These measurements provide the base for very accurate temperature profiles in the lower BL. In between the elevation scans, zenith observations were carried out at a temporal resolution of 1s. Thus, in between the accurate temperature profile determination, optimal estimates of humidity and LWC profiles are available on a high temporal resolution.

2.2. Active Instrumentation

The cloud radar data employed in this study was measured by the commercially available instrument MIRA36 operated by the University of Karlsruhe and built by METEK GmbH (http://www.metek.de/produkte.htm). It was stationed at the Falkenberg site from 16 September 2005 to 05 November 2005 only ~10 m away from HATPRO. MIRA36 is a pulsed radar operating at 36 GHz with a maximum sensitivity of -44 dBZ at 5 km at 0.1 s integration time. The vertical resolution used is 30 m up to a maximum height of 15 km. In this study the measurements of the radar reflectivity factor (Z) and Doppler velocity (v_d) are used for target classification and LWC profile retrieval.

The ceilometer deployed at Falkenberg during LAUNCH is a Vaisala LD40 of DWD with a temporal resolution of 15 s. This instrument measures a backscatter profile which is used to detect cloud base and to retrieve the extinction profile needed by K06. In this study for the lidar extinction profiles estimation we have used the inversion algorithm according to Klett (1981) that involves only one boundary value for the solution of the lidar equation: the absolute extinction on some reference level, which should be as far away from the lidar as possible. This method assumes a power-law relationship between range dependent lidar backscattering coefficient and optical extinction, where the exponent is considered to be unity for water clouds. (Rocadenbosch and Comeron, 1999 & Rogers et al, 1997). Lidar-ceilometers are more sensitive to small cloud particles than cloud radars, which in turn are highly sensitive to larger drops. Thus, lidar-ceilometer measurements are more accurate in deriving the actual cloud base height while cloud radars often detect light drizzle with negligible LWC below the actual cloud base. Also, often cloud radars are not sensitive enough to detect small droplets occurring in developing cumulus, which are, however, usually captured by lidar-ceilometers. Generally lidar-ceilometers cannot be used to detect the vertical cloud structure because most liquid water clouds are optically thick in the optical region of the spectrum such that the lidar-ceilometer signal will almost always be extinguished in the lower part of the cloud.

2.3. In-situ Measurements

The Lindenberg site has one of the longest historical data records of aerological measurements dating back to 1905. First height soundings were performed with kites reaching altitudes of up to ~10 km (Neisser and Steinhagen, 2005). Still today, a research focus is on vertical soundings of the atmosphere and thus radiosondes are launched 4 times daily at 0000, 0600, 1200 and 1800 UTC. Additionally, at the Falkenberg site, DWD maintains a 99 m mast with continuous measurements of temperature and humidity taken at six levels (10, 20, 40, 60, 80 and 98 m) with an integration time of 10 min.

3. Retrieval Method

The true atmospheric state vector $\mathbf{x}$ - to be retrieved in this study - consists of vertical profiles of atmospheric temperature ($\mathbf{T}$), absolute humidity ($\boldsymbol{\rho}_\mathbf{v}$) and cloud liquid water content ($\mathbf{LWC}$), such that we can notate $\mathbf{x}=(\mathbf{T}, \boldsymbol{\rho}_\mathbf{v}, \log_{10}(\mathbf{LWC}))$. From here on vectors will be noted in bold (here i.e. profile vectors). We retrieve $\log_{10}(\mathbf{LWC})$ instead of directly $\mathbf{LWC}$, because the distribution of $\log_{10}(\mathrm{LWC})$ more closely resembles a Gaussian shape than LWC and additionally, we do not have to worry about negative LWC values within the retrieval procedure. Multiple liquid water cloud layers can also be retrieved and state no limitation to the method. The vertical grid of T and ρ_v is set to 50 m in the lowest 200 m and then increases gradually to 150 m at 1000 m, 250 m at 3000 m and 500 m at 10 km above the surface –

corresponding approximately to typical height grids in state-of-the-art NWP. LWC, however, is retrieved on the vertical grid of the target classification.

3.1. Measurement Inversion

The goal of the IPT is to retrieve $\mathbf{x}$ by optimally exploiting the information from a given measurement vector $\mathbf{y}$ (Rodgers, 2000). Depending on the situation, $\mathbf{y}$ will consist of a specified vector of brightness temperatures **TB** and, in the cloudy cases, additionally of a vector of radar reflectivities **Z**, i.e. $\mathbf{y} = (\mathbf{TB}, \mathbf{Z})$. Principles of the method are described in detail by L07 and L04; here we want to focus on the improvements made in the last years and will thus only give a short method overview.

Generally in remote sensing applications, determining $\mathbf{x}$ from $\mathbf{y}$ directly is an underdetermined and ill-conditioned problem, meaning that no unique solution exists and that very small errors in the measurement may lead to huge deviations in the derived atmospheric profile. A way to solve this problem is to add *a priori information*, i.e. information about the atmospheric state which is given *prior* to the measurement, e.g. climatological information or data from the closest radiosonde. Typically, the optimal estimation equations (e.g. Rodgers 2000) are used for combining measurement and a priori information. If the relationship between $\mathbf{x}$ and $\mathbf{y}$ is slightly to moderately non-linear, an optimal atmospheric state $\mathbf{x}_{op}$ can be found by iterating the following formulation

$$\mathbf{x}_{i+1} = \mathbf{x}_i + \left(\mathbf{K}_i^T \mathbf{S}_e^{-1} \mathbf{K}_i + \mathbf{S}_a^{-1}\right)^{-1} \times \left[\mathbf{K}_i^T \mathbf{S}_e^{-1}\left(\mathbf{y} - \mathbf{y}_i\right) + \mathbf{S}_a^{-1}\left(\mathbf{x}_a - \mathbf{x}_i\right)\right] \quad (1)$$

where i represents the iteration step, $\mathbf{x}_a$ the a priori profiles of T, ρ_v and LWC, $\mathbf{S}_a$ the *a priori* covariance matrix and $\mathbf{S}_e$ the combined measurement and forward model error covariance matrix. $\mathbf{K}_i = \partial \mathbf{F}(\mathbf{x}_i)/\partial \mathbf{x}_i = \partial \mathbf{y}_i/\partial \mathbf{x}_i$ represents the so-called Jacobian, or the sensitivity of the forward model to changes in $\mathbf{x}$, whereby $\mathbf{K}_i$ is re-calculated for each iteration. The forward model $\mathbf{F}$ transforms from the state space ($\mathbf{x}$) to the measurement space ($\mathbf{y}$) in a straight-forward way. E.g., given a space vector at a certain iteration $\mathbf{x}_i$, **F** calculates **TB** by applying the Radiative Transfer Operator (RTO) at the HATPRO frequencies and, in the cloudy case only, **Z** by assuming a specified *Z*-LWC power law relationship of the form $Z = a\ \mathrm{LWC}^b$. Thus, the forward model can be noted in the following way:

$$\mathbf{F}(\mathbf{x}) = \begin{Bmatrix} \mathrm{RTO}(\mathbf{T}, \mathbf{q}, \mathbf{LWC}) \\ a \cdot \mathbf{LWC}^b \end{Bmatrix} = \begin{Bmatrix} \mathbf{TB} \\ \mathbf{Z} \end{Bmatrix} = \mathbf{y} \qquad (2)$$

Optimally, the formulation of Eq. 1 should guarantee the minimization of a quadratic cost function between $\mathbf{x}_a$ and $\mathbf{x}_i$, respectively $\mathbf{y}$ and $\mathbf{y}_i$, when the difference between $\mathbf{x}_{i+1}$ and $\mathbf{x}_\mathrm{i}$ goes towards zero. The iteration procedure is terminated after an optimal number of iterations (i=op) when IPT has converged to a sensible point. Here a quadratic cost function is applied to determine whether the retrieved $\mathbf{F}(\mathbf{x}_{op})$ is adequately close to the $\mathbf{F}(\mathbf{x}_{i-1})$ of the prior iteration (for more on the convergence criterion see L04). It is important to note that the solution $\mathbf{x}_{op}$ must be interpreted as the most probable solution of a Gaussian distributed probability density function, whose covariance can be written as:

$$\mathbf{S}_{op} = \left(\mathbf{K}_i^T \mathbf{S}_e^{-1} \mathbf{K}_i + \mathbf{S}_a^{-1}\right)^{-1}. \qquad (3)$$

The diagonal elements of this matrix give an estimate of the mean quadratic error of $\mathbf{x}_{op}$, whereas the off-diagonal elements yield information on the correlation of retrieval errors between the different heights.

A further important measure for retrieval algorithm evaluation is the averaging kernel matrix **A** which states the sensitivity of the retrieved to the true state (= $\partial\mathbf{x}_{op}/\partial\mathbf{x}$). In the case of Gaussian statistics, **A** can be written as

$$\mathbf{A} = \mathbf{S}_{op} \cdot \left(\mathbf{K}_i^T \mathbf{S}_e^{-1} \mathbf{K}_i\right). \qquad (4)$$

The diagonal values of $\mathbf{A}$ are frequently used as a measure of vertical resolution (Rodgers, 2000) whereas the trace of $\mathbf{A}$ states the independent number of levels which can be retrieved from a given measurement.

3.2. Target Classification

The current IPT version described in this study is not applicable to atmospheric columns containing significant precipitation as well as columns with ice and liquid phase occurring at one level. In the first case problems with the instruments' performance occur (e.g. wet MWP radome or radar attenuation effects), whereas in the latter case the radar cannot easily distinguish the contributions of ice and liquid water to Z.

In order to identify regions where and where not the IPT can be applied, we have employed the Cloudnet (Illingworth et. al, 2007) target classification scheme developed at the University of Reading, UK. This scheme classifies the targets, which contribute to the backscattered radiation received either by the cloud radar or the lidar ceilometer (Fig. 1). With this classification scheme it is possible to discriminate if the backscattered radiation originates e.g. from liquid clouds, ice clouds, precipitating or non-precipitating clouds or even aerosols or insects. The radar and lidar observations are first averaged to a common grid (i.e. 30 s in time and 60 m in height) and then supplemented by temperature, pressure, humidity and wind speed from an operational NWP model to assist with attenuation correction and cloud phase identification. The full details of how the backscatter targets in each radar/lidar pixel are then categorized into a number of different classes are given by Hogan and O'Connor (2006), but essentially we make use of the fact that radar is sensitive to large particles such as rain and drizzle drops, ice particles and insects, while the lidar is sensitive to higher concentrations of smaller particles such as cloud droplets and aerosol. We define drizzle as water droplets greater than 50 μm in diameter, which have a significant fall terminal fall velocity. The terminal fall velocity of the smaller cloud droplets (diameters less than 50 μm) is typically only a few cm s^{-1}. Additionally, the high lidar backscatter of liquid droplets also enables *super-cooled* liquid layers to be identified even when embedded within ice clouds (Hogan et al. 2003).

3.3. Clear Sky Mode

If the target classification identifies a profile without any clouds or the detected cloud layers consist of pure ice phase, the "clear-sky" mode is used to retrieve the atmospheric state vector $\mathbf{x} = (\mathbf{T}, \boldsymbol{\rho}_v)$. Note that the employed microwave frequencies show no sensitivity to non-precipitating ice clouds. To optimally exploit the capabilities of HATPRO concerning T-profiling, the measurement vector consists not only of the 14 zenith-pointing TBs of all HATPRO channels, but additionally of 20 TBs at five off-zenith elevation angles (θ=42.0, 30.0, 19.2, 10.2, 5.4) at the four HATPRO channels 11-14 (ν = 54.94, 56.66, 57.30, 58.00 GHz) adding up to a total of 34 TB values. Because the atmosphere is close to optically thick at 55-58 GHz, the lower elevation angles add more information content on the lower part of the atmospheric temperature profile than the higher elevation angles and vice versa. This effect, together with the height resolution contained in the frequency dependent measurements, leads to an enhanced vertical resolution of the BL temperature profile. The six angles correspond to air mass factors of ~ 1, 1.5, 2, 3, 6 and 10 and were originally chosen in order to optimize statistical retrievals of T-profiles (Crewell and Löhnert, 2007).

To practically rule out the possibility of HATPRO being influenced by a cloud at an off-zenith elevation angle, the ceilometer time series of lowest cloud base at ±20 min around the time of measurement is analyzed. In case there are no clouds detected within this time interval, we assume the atmosphere is horizontally stratified. It must be mentioned, that in a small percentage of cases, this assumption may be wrong due to persistent cloud structures occurring at a fixed position relative to the measurement site. In future this uncertainty may be accounted for by using a simultaneous scanning infrared radiometer. For the case that a cloud is detected, the *lowest* cloud base detected in this period is compared to a threshold value derived from a TB climatology (Tab. 1). This climatology is based on a 10-year radiosonde data set of Lindenberg including the years 1996 – 2005 with operational launches at 0000, 0600, 1200 and 1800 UTC. It contains simulated TBs at all elevation angles calculated with (TB_{cloud}) and without liquid clouds (TB_{clear}). Liquid clouds have been placed within the radiosonde ascent using a threshold value of 95% in humidity and a modified adiabatic assumption (Karstens et al. 1994). For a given elevation angle-frequency combination, the scatter of cloud base versus ΔTB (=$|TB_{cloud}$-$TB_{clear}|$) shows the influence of a cloud at a certain height to the observed TB. Based on these statistics we determine a critical cloud base threshold to include only those off-zenith TB observations (of the originally 20 off-zenith TB observations) in the retrieval where the lowest observed cloud base indicates a ΔTB of less than 0.1 K (Tab. 1). In case of a clear sky observation in the zenith, but the occurrence of a cloud base of lower than 69 m in the +-20 min time window around the zenith observation, this would mean excluding the elevation angles 42°, 30°, 19° at 54.94 GHz. Sensitivity studies showed that the temperature retrieval accuracy in this case is reduced no more than 0.1 K throughout the profile in comparison to the case when using all angle-frequency combinations.

For the retrievals applied to the elevation scans, the a priori profile $\mathbf{x}_a$ consists of the temporally interpolated profiles of temperature and humidity using only the 0000 and 1200 UTC Lindenberg radiosonde ascents. The $\mathbf{S}_a$ matrix is then calculated by evaluating the temporally interpolated profiles at 0600 and 1800 UTC against the actual 0600 and 1800 UTC ascents Lindenberg ascents using the 10-year radiosonde climatology. Thus, the diagonal of $\mathbf{S}_a$ will contain the variance of this difference and the off-diagonal components the corresponding covariances. The larger the diagonal components, the less weight is given to $\mathbf{x}_a$ in the retrieval process and vice-versa.

Between two subsequent elevation scans only zenith TBs are available, so that the measurement vector will only consist of 14 values. Due to the expected higher **T**-accuracy from the elevation scan retrievals, **T** derived from the latest available elevation scan is taken as the temperature a priori profile between two subsequent scans. For the temperature part, the covariance matrix $\mathbf{S}_a$ is set to the error covariance matrix $\mathbf{S}_{op}$ (Eq. 3), which describes the uncertainty of the retrieved profile. For $\boldsymbol{\rho}_v$ the a priori information is always taken from the statistics of the temporally interpolated radiosonde profiles.

3.4. Cloudy Sky Mode – LWC calculation

The target classification scheme allows the identification of the liquid cloud regions within the profile. If this is the case, the assumption of a horizontally stratified atmosphere is again no longer given due to the strong variability connected with clouds. To still be able to make use of the elevation scans, the same cloud base threshold method as described in section 3.3 is applied. Also the a priori assumptions for **T** and $\boldsymbol{\rho}_v$ are identical to the ones applied to the clear sky mode.

K06 Method for LWC profiling

In order to infer LWC from the radar reflectivity *Z*, a power law relationship $Z = a\,\mathrm{LWC}^b$ is often used (e.g. Fox and Illingworth, 1997) with fitting parameters *a* and *b*. Typically, for non-precipitating clouds, Rayleigh scattering conditions are given meaning that *Z* is equal to the 6$^{\text{th}}$ moment of the drop size distribution (DSD). However this also means that a small number of larger particles (i.e. drizzle) can contribute to the major part of the *Z* without a strong contribution to the LWC and the effective radius. A typical *Z*-LWC diagram calculated from DSD measured in-situ from aircraft during four field campaigns is presented in Fig. 2a. It shows up to 40 dB variability in *Z* for a fixed value of LWC. Using the ratio Z/α between the radar reflectivity *Z* and ceilometer optical extinction α as a discriminating parameter, K06 and Krasnov and Russchenberg (2002) have developed a technique, which discriminates between 3 categories of water clouds – "without drizzle" (the drizzle fraction contribution to radar reflectivity *Z* and LWC is negligible and the DSD can be described by a standard modified gamma or log-normal three parameter distribution), "light drizzle" (the drizzle fraction dominates *Z*, but its contribution to LWC is less then 0.03 g m^{-3}) and "heavy drizzle" (*Z* is completely determined by the drizzle fraction and its contribution to LWC is significant, whereby the DSD is characterized as a mixture of two independent distributions). For each category a specific *Z*-LWC power law (i.e. different *a*, *b* coefficients) is derived (see Figs. 2b-d and Tab. 2).

If the lidar signal within the cloud is attenuated and no radar-to-lidar ratio Z/α is available, *Z* thresholds (-35 and -20 dBZ) are used to determine the water cloud category. These thresholds are derived from simultaneous cloud measurements of radar and lidar with known lidar optical extinction using the extensive Cloudnet database archive from the four European sites Cabauw (NL), Chilbolton (UK), Palaiseau (F) and Lindenberg (D).

Once the water cloud category has been identified via Z/α or *Z* threshold, the appropriate coefficients *a* and *b* are chosen and are then used within the forward model **F** (Eq. 2) to calculate LWC within the retrieval procedure. The accuracy of each of the derived *Z*-LWC relationships is also derived from the in-situ data of the four field campaigns shown in Fig. 2. This is done by applying the derived *Z*-LWC relationship to the in-situ determined value of *Z* and then calculating the mean square difference of the retrieved LWC to the actually measured LWC. Hence, the corresponding diagonal components of $\mathbf{S}_e$ are determined.

LWC a priori profile

In contrast to L04, where a mean LWC profile derived from multiple singular column cloud model runs is used as a priori, the LWC a priori profile used here is calculated using a modified adiabatic approach (Karstens et al. 1994). The main advantage is that no restrictions concerning cloud vertical extension as in L04 (maximum cloud extension of 1500 m) and vertical resolution (formerly 250 m) apply. This approach is applied to all height levels containing the cloud categories "without drizzle" and "light drizzle" from K06. Generally, the liquid water content as calculated for an adiabatic ascent (LWC_{ad}), (e.g. Rogers and Yau (1989)), is assumed to be the maximum possible LWC and is corrected for effects of dry air entrainment, freezing drops or precipitation in the modified adiabatic approach. The empirical correction function used was derived from aircraft measurements of LWC in different types of non-precipitating clouds (Warner 1955)

$$\mathrm{LWC} = \mathrm{LWC}_{ad}\left(1.239 - 0.145\ln(h)\right) \quad (5)$$

with h in m indicating the height above cloud base and h within the range between 1 m and 5140 m.

As a further constraint to minimize the degrees of freedom, the humidity is set to its saturation value within the detected cloud boundaries. The saturation value of ρ_v in a specific cloud layer is determined using the corresponding T value of the prior iteration. For the first iteration, the first guess value of T is used.

4. IPT Application to simulated cases

In this section we would like to show the accuracy improvements achieved by including the elevations scans for the retrieval of temperature profiles. This is done on the basis of a simulation study for clear sky situations when the strongest temperature variations are expected due to strong radiative fluxes at the surface. Löhnert et al. (2007) have performed an extensive accuracy assessment of the IPT within a NWP model domain using zenith measurements only, so this will not be the main focus of this section. Here radiosonde ascents from Lindenberg identified as "clear sky" of the years 1997 and 2002 (in total 1130 ascents) are used to calculate the 34 HATPRO TBs (section 3.3) needed for boundary layer profiling for each radiosonde ascent. Here, we use a radiative transfer model according to Czekala and

Simmer (2002) together with a Fast Absorption Predictor (FAP) based on the absorption model by Rosenkranz (1998) to calculate the absorption coefficients of the relevant gaseous components (oxygen, water vapour and nitrogen) in the microwave region (for more details on FAP see L04). The absorption coefficient for liquid water is calculated in a straight forward way using the model according to Liebe (1993). A channel dependent Gaussian noise factor to account for radiometric noise and random calibration uncertainty is added to the simulated TBs on the basis of HATPRO clear sky observation during periods of low variations in total atmospheric water vapour amount (IWV). On this basis the channels 1 – 7 are assigned with a noise factor of 0.4 K, channels 8 – 10 with 0.5 K and channels 11 – 14 (including the elevation scans) with 0.2 K. During an elevation scan, the uncertainties of the measurements at one and the same frequency but at different elevation angles are probably not independent. Currently we have not included this fact in the calculation of the $\mathbf{S}_e$ matrix – the instrument uncertainties are only included in the diagonal components of $\mathbf{S}_e$. This may have small influence on the error characteristics or even the vertical resolution of the retrieval results.

In order to evaluate the IPT performance, the retrieved **T** is compared to the true **T** profile, but also to the a priori profile, which consists of the temporally interpolated radiosonde profile (section 3.3). Thus, the comparisons show us which accuracy is gained by adding the HATPRO measurements to the a priori information. Results are shown for two IPT runs: one using all 34 TBs, including the elevation scans of the channels 11, 12, 13 and 14 (IPT_ELE) and the other using the 14 zenith observed TBs only (IPT_ZEN). Note that the channels 1 – 7 are used in both retrievals because the humidity profile is retrieved simultaneously to the temperature profile. Compared to the a priori profile, the increase in (Root Mean Square) RMS accuracy is the most pronounced near the surface and decreases to the order of 0.1 K above 2 km height (Fig. 3a) for both IPT_ZEN and IPT_ELE. Above this height the information added to the retrieval by remote sensing is nearly zero. Close to the surface a slight negative BIAS in the temperature a priori profile occurs which can be compensated both by IPT_ZEN und IPT_ELE. IPT_ELE shows RMS accuracies as low as 0.3 K close to ground and lower than 1 K in the lowest 3 km. In the lowest 2 km the average RMS accuracy of IPT_ZEN is 0.85 K and of IPT_ELE 0.59 K, whereas the a priori profile shows an accuracy of 1.43 K. IPT_ELE outperforms IPT_ZEN on average by 0.26 K in the lowest 2 km. Above this height the influence of the elevation scans is no longer significant.

Starting from the a priori estimate for the actual humidity profile (RMS accuracies are less than 1.1 gm^{-3} throughout the profile), both IPT versions enhance the average RMS accuracy in the lowest 5 km from 0.77 to 0.60 gm^{-3} (Fig 3b). The influence of the remote sensing observations extends to higher levels than in the temperature case due to the fact, that the humidity weighting functions of the Band A channels are approximately constant with height. Note that, as expected, no significant differences are observed between IPT_ZEN and IPT_ELE in case of the humidity retrieval.

The increase in temperature RMS accuracy below 1 km is especially relevant for resolving boundary layer inversions (BLI). To evaluate the BLI cases, we have analyzed all profiles containing a temperature increase with height over layers of at least 100 m (667 out of 1130 cases). As shown by a typical near-surface BLI example, IPT_ELE reproduces **T** much more realistically than IPT_ZEN (Fig. 4a). The average RMS accuracy of IPT_ZEN is 0.95 K and of IPT_ELE 0.59 K for all BLI cases in the lowest kilometer above the ground (Fig. 4b). In comparison to all analyzed cases, the accuracy of IPT_ZEN decreases, whereas the IPT_ELE accuracy stays constant, underlining the strength of IPT_ELE in retrieving BLIs.

The T-retrieval performance of IPT_ELE in contrast to IPT_ZEN can also be regarded in terms of number of independently retrievable layers. Generally IPT_ELE shows a higher ability to resolve T perturbations with the number of independent levels of IPT_ELE and IPT_ZEN being 3.3, respectively 1.7 (=tr($\mathbf{A}$), see Eq. 4). This underlines the need for including elevation scans into microwave profiler retrievals of **T**. For the humidity retrieval, the number of independent layers is dependent on the total water vapour amount in the atmosphere, whereby the numbers range from 1.2 (low IWV) to 1.5 (high IWV).

5. Evaluation of IPT retrievals during LAUNCH

The IPT_ELE, as described in the sections above, has been continuously applied to the measurements gathered at the Falkenberg remote sensing site during LAUNCH. In this application we retrieve **T**, $\boldsymbol{\rho}_v$ and **LWC** by employing the method as described in section 3.4. The retrievals are derived for 19 October 2005 – 31 October 2005, which was the only time period when all the required instruments (i.e. microwave profiler, cloud radar and ceilometer) were measuring simultaneously and without error. In total 7324 thermodynamic profiles have been calculated. The first two days of the period were characterized mostly by dry weather, with occasionally scattered low level liquid clouds and some cirrus aloft. During 21 October – 25 October frequent rain events dominate, with convective activity reaching up to 11-12 km (21st, 25th) or long-lasting stratiform events (24th). During these periods IPT is not applicable due to water on the radome of the microwave profiler leading to measurements that are not interpretable. The last 6 days of the period are then characterized by a rather stable high pressure period with some scattered BL cumulus on the 26th and 27th and no BL clouds from the 28th to the 31st.

5.1. Comparison with mast observations

The mast measurements of T and ρ_v at the Falkenberg site, which are averaged on a 10 min temporal grid, present an excellent possibility of evaluating the IPT results in the lowest 100 m. The obtained results from 19 October – 31 October are shown in Fig. 5, each evaluated at 50 m and 100 m above ground, which correspond to two of the three lowest levels in the IPT vertical grid. For the 100 m comparison, the highest mast measurement (98 m) was used, whereas the 50 m value was obtained by averaging the 40 and 60 m mast values. The RMS differences between mast and IPT are very satisfactory and on the order of 0.5 – 0.6 K, with negligible BIAS errors. Considering the random error of the mast measurements (~0.1 K) as well as retrieval errors due to horizontal variations in the temperature field (~0.2 K), these results agree very well with the predicted errors from the simulation experiment state applying elevation scans. Since these simulation results were significantly lower than the IPT errors resulting from the zenith-only mode (section 4), we conclude that the real measurements also significantly benefit from the elevation scan procedure. It must be mentioned, that these satisfactory retrieval results in the lower BL are largely due to the capability of moving the elevation scan down 10.2° and even 5.4° above the horizon. This was only possible due to the very flat terrain surrounding the Falkenberg measurement site. Compared to the retrieval of *T*, the IPT performance with respect to ρ_v is not as convincing (Fig. 5), mainly due to the fact that the height resolution is much poorer (section 4). The RMS differences between mast and IPT are of the order of 0.8 gm^{-3}. These RMS values are slightly (0.1 - 0.2 gm^{-3}) larger than the expected values from the simulation and additionally BIAS errors on the order of 0.5 gm^{-3} occur. Next to horizontal humidity variations and random error of the mast measurements, we expect unaccounted systematic calibration uncertainties of the tower sensor and microwave profiler itself, as well as unknown errors of the microwave absorption model to be causing these errors.

5.2. Analysis of temperature time series

In this section we analyze the IPT derived temperature time series in comparison to the radiosonde and the LME model output (Figs. 6 and 7). Particularly, temporally highly resolved developments of lowest boundary layer (0-500 m) are well represented in the IPT (Fig. 6b), whereas these developments are naturally not detectable in the interpolated 12-hourly radiosonde time series (Fig. 6a). For example, the strength of the stable nocturnal BL inversion on the clear-sky days (19th, 27th-31st) is underestimated (Fig. 6f). The transition from a stable to a well mixed BL is also not recoverable by using the 12-hourly interpolated radiosonde profiles. This is expressed during daytime by the high positive deviations in Fig. 6f. The overestimations of the radiosonde with respect to the IPT temperatures occurring during the well mixed BL in 500 – 1000 m also indicate that the gradient of the temperature profile is not strong enough (i.e. less than 1 K/100m through the BL). The vertical "stripe-like" structures seen in Fig. 6f occurring mainly in 1 to 3 km height must still be examined more closely in future. We assume them to origin from a combination of radiometric noise and horizontal inhomogeneities. However, in order to check the possibility of real temporal variations in the vertical temperature profile, we plan to assess Raman lidar and/or tethered balloon measurements during future campaigns (e.g. COPS 2007, http://www.uni-hohenheim.de/cops/) which will give us independent and continuous temperature measurements aloft. With the available data, it is currently not possible to evaluate these effects conclusively.

The above mentioned characteristics can also be identified when analyzing the mean diurnal cycle of the five clear-sky days in (Fig. 7), where the interpolated radiosonde temperature amplitude is not able to follow the retrieved amplitude of the 12-hourly sondes. Note that the radiosonde and IPT match at ~1100 UTC and not at 1200 UTC due to fact that the radiosondes are generally launched ~45 min before scheduled time in order to account for the duration of the ascent. Fig. 7a and 7b also nicely show the correspondence between the mast measurements and IPT, which could be expected from the results discussed in section 5.1.

Potential for model evaluation

The potential of an IPT like method to evaluate the performance of a numerical weather prediction model is also shown in Figs. 6 and 7. A precise representation of the BL is essential in state-of-the-art numerical weather forecast models for correctly modeling convection, clouds and regional precipitation events. An evaluation of the performance of such models in the BL is thus of extreme importance and cannot be carried out using twice-daily operational radiosonde data as demonstrated above. A combination of instruments as used by the IPT may prove very valuable when comparing long-term time series of thermodynamic profiles with model output from NWP. Microwave profiler, cloud radar and ceilometer together provide a unique combination for the simultaneous retrieval of temperature, humidity and cloud liquid water profiles with the respective error bars.

To show the potential for NWP evaluation we have also analyzed temperature fields of the Lokal Modell (LME) of the German Weather Service calculated for the LAUNCH campaign in a 24h forecast mode, with model runs commencing at 0000 UTC. Comparisons of these forecasts with the interpolated radiosonde and the IPT retrievals are shown in Fig. 6. As can be seen in Fig. 6d, LME represents the development of the lowest boundary layer more accurately than the interpolated radiosonde, i.e. its behavior is very similar to that of the IPT. This characteristic can also be seen in the mean diurnal cycle of the lowest temperatures (Fig. 7 and the 50 and 100 m level). However, the comparison at the 50 m level also shows that the model overestimates the lowest temperature of the stable nocturnal BL in the early morning hours with ~ 1K, whereas the decay of the well mixed daytime BL is too quick and model temperatures are ~1.5 K too low at the end of the day. At 400 m the model shows a more uniform mean temperature cycle than the IPT, with the tendency of too low temperatures in the morning and too high temperatures in the afternoon. Fig. 6 shows further interesting phenomena which can be analyzed by comparing IPT – LME. E.g. before noon time on October 31st the boundary layer inversion was almost overcome in the model, but not nearly in the measurements. Also interesting are the discrepancies concerning the development of the BL inversion at mid to end of the 27th, where LME overestimates T on the order of 3 K from 500 to 1500 m (also visible in the RS comparison).

It must be mentioned that these comparisons only encompass 6 clear-sky days and should not be interpreted in a representative way. However, we do want to underline the potential of an IPT like procedure for evaluating NWP for future applications.

5.3. LWC profile retrieval

The mean profiles of LWC calculated are shown in Fig. 8 as a function of height above cloud base. Fig. 8 shows the results for clouds with vertical extensions up to 400 m binned in 100 m steps. Retrievable clouds with vertical extensions larger than 400 m are not shown in Fig. 8 due to their very seldom occurrence. Of the 7324 calculated profiles, 2391 profiles were identified as cloudy. We show results of LWC derived with the IPT for cloudy cases described in section 3.4 and compare them to the method according to K06. Note that K06 has been incorporated into IPT, but results still differ due to the fact that the IPT results not only rely on *Z*, but also on the LWC a priori profile and the MWP brightness temperatures.

The mean LWP difference between IPT and K06 is -1.4 gm^{-2} showing a relatively good agreement with respect to a total mean IPT-LWP of ~36.9 gm^{-2}. However, the RMS difference between both methods is ~45 g m^{-2} showing the need for a more extensive evaluation of the LWC profiles. This is, however, a difficult task since the truth is not available. L07 report a IPT-LWP RMS error of ~6 g m^{-2} using simulated data and additionally this was achieved for non-precipitating clouds only. In order to finally assess the accuracy of IPT and K06, studies employing cloud models with spectrally resolved cloud microphysics must be carried out in future. The shapes of the mean IPT and K06 profiles are also completely different for all four vertical extensions. This is mainly due to the fact that for the cloud class "non-drizzling" and "light drizzle" the IPT procedure uses the modified adiabatic profile assumption (see section 3.4) as a priori information, which shows an increasing LWC with height above cloud base. For the cloud class "heavy drizzle" no a priori assumption for the LWC profile is made because a cloud with significant drizzle is not necessarily expected to show an adiabatic like behavior.

6. Conclusions

This study has demonstrated advances in profiling the vertical thermodynamic structure of the boundary layer by extending the Integrated Profiling Technique of L04 with elevation scan information from the MWP, a sophisticated target classification scheme and a radar-lidar method (K06) to retrieve LWC also within drizzling clouds. Thus, the IPT is now suited for accurately retrieving the development of boundary layer inversions together with a more generally applicable retrieval of liquid clouds in the BL. The evaluation of long-term IPT time series has a very high potential for the evaluation of NWP models but also for satellite retrievals, e.g. DWD Lindenberg is currently planning a METOP evaluation with IPT retrieval data and the Royal Dutch Meteorological Service is currently running the IPT at the remote sensing site Cabauw, NL to perform model validation and climatological studies. KNMI will also be running the Reading target classification scheme in a near real time mode shortly, so that advanced thermodynamic profiles will be continuously available. In this respect is must be mentioned, that the IPT can also be adapted to run in a "now-casting" mode using the latest available radiosonde as a priori information as demonstrated by L07.

However, more comparative studies must be carried out in order to finally characterize IPT performance, especially in heights above 1 km. Here *T* retrievals are especially sensitive to the absolute calibration of the MWP but also rely strongly on the microwave absorption model, where uncertainties in the O_2 line-coupling may account for retrieval errors (Boukabara et al., 2005). In this context, the Cabauw site is ideally suited for future IPT assessment: here KNMI operates a 35 GHz cloud radar, a HATPRO instrument and a ceilometer. It also has a 200 m tower, which will allow an IPT assessment during various weather regimes over long time intervals and the operational radiosonde site with two launches per day is only 30 km away – allowing at least an evaluation of systematic error in *T* and ρ_v retrievals. These studies will also help in investigating whether such measurements have potential for routine assimilation in NWP models. In this context, it is very helpful that the IPT resembles a 1D variational procedure, which also provides error estimates for every profile retrieval.

Future expansions of the IPT will consist of including measurements from infrared sensors (e.g. a radiometer in the 9-12 micrometer range or a highly spectrally resolving Atmospheric Emitted Radiance Interferometer - AERI). The retrievals will then also be made physically consistent with the infrared radiances leading to more accurate retrievals of low water content (< 30 gm^{-2}) liquid clouds, which are momentarily difficult to detect with HATPRO, but still have a large impact on the solar radiation balance.

Acknowledgements

We would like to thank the German Weather Service (DWD) at Lindenberg (especially Dr. Dirk Engelbart and Dr. Ulrich Goersdorf) for hosting the LAUNCH campaign and especially for providing the measurement infra-structure. LAUNCH was embedded in the European COST 720 action "Integrated Ground-Based Remote-Sensing Stations for Atmospheric Profiling", where the presented work was coordinated. We are grateful to Bernhard Pospichal and Dr. Jan Handwerker for setting up and operating HATPRO, respectively MIRA36. We also would like to thank Dr. Felix Ament (MeteoSwiss) for carrying out the LME calculations. The enhancement of the retrieval algorithm has been carried out within the framework of the DFG project "Application and validation of synergetic cloud property retrieval during the Tropical Warm Pool - International Cloud Experiment TWP-ICE" (GZ: LO 901/2-1). The study was also supported by the Netherlands Space Agency (SRON) and the Dutch National Research Program Climate Changes Spatial Planning.

References

Atlas, D., 1954: The estimation of cloud content by radar. *J. Meteor.*, **11**, 309-317.

Baedi, R. J. P., J. J. M. de Wit, H. W. J. Russchenberg, J. S. Erkelens, and J. P. V. Poiares Baptista, 2000: Estimating Effective Radius and Liquid Water Content from Radar and Lidar Based on the CLARE'98 Data-Set. *Phys. Chem. Earth (B)*, **25**, 1057-1062.

Boukabara, S., S.A. Clough, J. Moncet, A.F. Krupnov. M.Y. Tretyakov and V.V. Parshin: Uncertainties in the Temperature Dependence of the Line-Coupling Parameters of the Microwave Oxygen Band: Impact Study, 2005: *IEEE Trans. Geosci. Remote Sensing*, **43**, No. 5

Czekala, H. and C. Simmer, 2002: On precipitation induced polarization of microwave radiation measured from space. *Meteorol. Z.*, **11**, 49–60

Crewell, S., and U. Löhnert, 2007: Accuracy of boundary layer temperature profiles retrieved with multi-frequency, multi-angle microwave radiometry. *IEEE Trans. Geosci. Remote Sensing*, in press.

Fox, N. I., and A. Illingworth, 1997: The potential of a spaceborne cloud radar for the detection of stratocumulus. *J. Appl. Meteor.*, **36**, 676-687.

Hogan, R. J., and E. J. O'Connor, 2006: Facilitating cloud radar and lidar algorithms: the Cloudnet Instrument Synergy/Target Categorization product. Cloudnet documentation: *http://www.cloud-net.org/data/products/categorize.html*.

Hogan, R. J., A. J. Illingworth, E. J. O'Connor, and J. P. V. Poiares Baptista, 2003: Characteristics of mixed-phase clouds: Part II: A climatology from ground-based lidar. *Quart. J. Roy. Meteorol. Soc.*, **129**, 2117-2134.

Illingworth, A. J., R. J. Hogan, E. J. O Connor, D. Bouniol, M. E. Brooks, J. Delanoë, P. Donovan, J. D. Eastment, N. Gaussiat, J. W. F. Goddard, M. Haeffelin, H. Klein

Baltink, O. A. Krasnov, J. Pelon, J.-M. Piriou, A. Protat, H. W. J. Russchenberg, A. Seifert, A. M. Tompkins, G.-J. van Zadelhoff, F. Vinit, U. Willén, D. R. Wilson, and C. L. Wrench, 2007: CLOUDNET Continuous evaluation of cloud profiles in seven operational models using ground-based observations. *Bull. Amer. Meteor. Sci.*, in press

Kadygrov E. N., and D. R. Pick, 1998: The potential performance of an angular scanning single channel microwave radiometer and some comparisons with in situ observations, *Meteorological Applications,* **5**, 393-404

Karstens, U., C. Simmer, and E. Ruprecht, 1994: Remote sensing of cloud liquid water, *Meteorol. Atmos. Phys.*, **54**, 157-171

Klett, J. D., 1981: Stable analytical inversion solution for processing lidar returns. *Appl. Opt.*, **17**, 211-220.

Krasnov, O. A., and H. W. J. Russchenberg, 2002: The relation between the radar to lidar ratio and the effective radius of droplets in water clouds: an analysis of statistical models and observed drop size distributions. *The 11th Conference on Cloud Physics*, June 2-7, 2002, Ogden, UT, AMS.

Krasnov, O. A., and Russchenberg, H., 2006: A synergetic radar-lidar technique for the LWC retrieval in water clouds. *7th International Symposium on Tropospheric Profiling*, Boulder, Colorado, USA, June 11-17, 2006

Liebe, H. J., G. A. Hufford, and M. G. Cotton, 1993: Propagation modelling of moist air and suspended water/ice particles at frequencies below 1000 GHz. *Atmospheric Propagation Effects through Natural and Man-Made Obscurants for Visible through MM-Wave Radiation*. AGARD-CP-542, 3.1-3.10.

Löhnert, U., E. van Meijgaard, H. Klein Baltink, S. Groß, and R. Boers, 2007: Accuracy assessment of an integrated profiling technique for operationally deriving profiles of temperature, humidity and cloud liquid water. *J. Geophys. Res.*, **112**, D04205, doi:10.1029/2006JD007379

Löhnert, U., S. Crewell, and C. Simmer, 2004: An integrated approach towards retrieving physically consistent profiles of temperature, humidity, and cloud liquid water. *J. Appl. Meteor.*, **43**, 1295-1307

Löhnert, U., and S. Crewell, 2003: Accuracy of cloud liquid water path from ground-based microwave radiometry, Part I: Dependency of cloud model statistics. *Radio Sci.*, **38**, 8041, doi:10.1029/2002RS002654.

Neisser, J, and H. Steinhagen, 2005: Die Historie des MOL 1905–2005, *Promet*, **31**, Nr. 2–4, available from http://www.dmg-ev.de/gesellschaft/publikationen/pdf/promet

Rocadenbosch, F. and A. Comeron, 1999: Error Analysis for the Lidar Backward Inversion Algorithm. *Appl. Opt*, **38**, 4461-4474

Rodgers, C. D., 2000: *Inverse methods for atmospheric sounding: Theory and practice*. World Scientific, 238 pp.

Rogers, R. R., M.-F. Lamoureux, L. R. Bissonnette, R. M. Peters, 1997: Quantitative Interpretation of Laser Ceilometer Intensity Profiles. *J. Atmos. Oceanic Technol.*, **14**, 396 - 411

Rogers, R. R., and M. K. Yau, 1989: A short course in cloud physics, Butterworth-Heinemann, Woburn, MA, USA, 290 pp

Rose, T., S. Crewell, U. Löhnert, and C. Simmer, 2005: A network suitable microwave radiometer for operational monitoring of the cloudy atmosphere. *Atmos. Res.*, Special issue: CLIWA-NET: Observation and Modelling of Liquid Water Clouds, **75**, 183-200, doi:10.1016/j.atmosres.2004.12.005.

Rosenkranz, P. W., 1998: Water vapour microwave continuum absorption: A comparison of measurements and models. *Radio Sci.*, **33**, 919–928.

Warner, J., 1955: The water content of cumuliform clouds. *Tellus,* **7**, 449-457.

Figure Captions

Fig. 1: An example 24-hour time series of the target classification scheme (Lindenberg, 22 October 2005) according to Hogan and O'Connor (2006). A target classification index is given below.

Fig. 2: Two-dimensional diagrams of the *Z*-LWC relation derived from in-situ aircraft data from four different field campaigns (see also Tab. 2); (a) – all analysed datasets, (b) – for the cloud "without drizzle" (F), (c) – for the cloud "light drizzle" (B), and (d) – for the cloud "heavy drizzle" (K). The categorization has been carried using the radar reflectivity to lidar optical extinction ratio: (b) $\log_{10}(Z/\alpha)$ < -1; (c) -1 < $\log_{10}(Z/\alpha)$< 1.8; and (d) $\log_{10}(Z/\alpha)$> 1.8 (according to K06). In (b)-(d) the dashed line represents the derived *Z*-LWC relationship, the bold line the average *Z* value for a given LWC and the dotted line the corresponding standard deviation.

Fig. 3: Temperature (3a, left) and humidity (3b, right) BIAS and RMS errors for IPT application to simulated radiances from 1130 clear-sky radiances. The dashed (IPT_ZEN) and dashed-dotted (IPT_ELE) show the results using only zenith TB observations, respectively zenith and elevation scanning observations. Additionally shown are the errors of the a priori profile, which states the linear interpolation between two 12-hourly radiosondes. Note that in the humidity plot IPT_ZEN and IPT_ELE cannot be differentiated because they show nearly the same values.

Fig. 4: (a, left): Performance of IPT_ELE and IPT_ZEN in a strong low-level inversion case compared to the radiosonde (RS). (b, right): BIAS and RMS errors of IPT_ZEN and IPT_ELE applied to all the simulated data (Fig. 3) showing boundary layer inversion.

Fig. 5: Comparisons of IPT and mast measurements of temperature (top) and humidity (bottom) at levels 50 and 100 m above ground.

Fig. 6: Time series of temperature and cloud base (black dots) in the lowest 3 km between 19 October and 31 October 2005. (a): interpolated radiosonde profiles (12 hourly), (b): retrieved IPT profiles, (c): LME model profiles. Also: Time series of temperature difference

(d): interpolated radiosonde – LME profiles (e): IPT – LME profiles, (f): IPT – interpolated radiosonde profiles. Radiosonde ascent times are marked “x”. The vertical white bands denote times when the IPT could not be applied, mostly due to missing data of one of the instruments, precipitation, not fulfilled convergence criteria or radiometer calibration.

Fig. 7: Mean diurnal cycle of temperature derived during the 5 practically cloud-free days 27-31 October 2005 during LAUNCH for the different measurement-types IPT, radiosonde (RS) and mast in comparison to the 24-h LME forecasts initialized at 0000 UTC. Results at 400 m do not include any mast measurements

Figures:

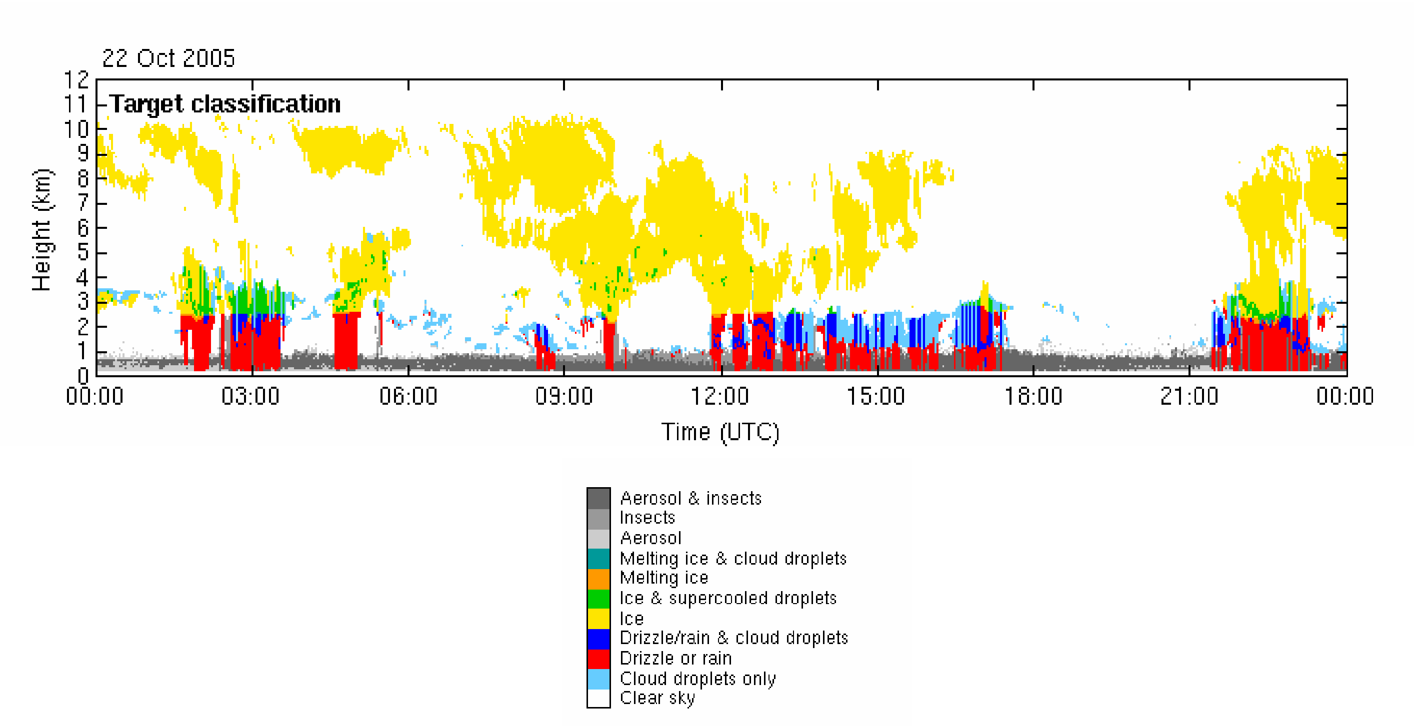

Fig. 1: An example 24-hour time series of the target classification scheme (Lindenberg, 22 October 2005) according to Hogan and O'Connor (2006). A target classification index is given below.

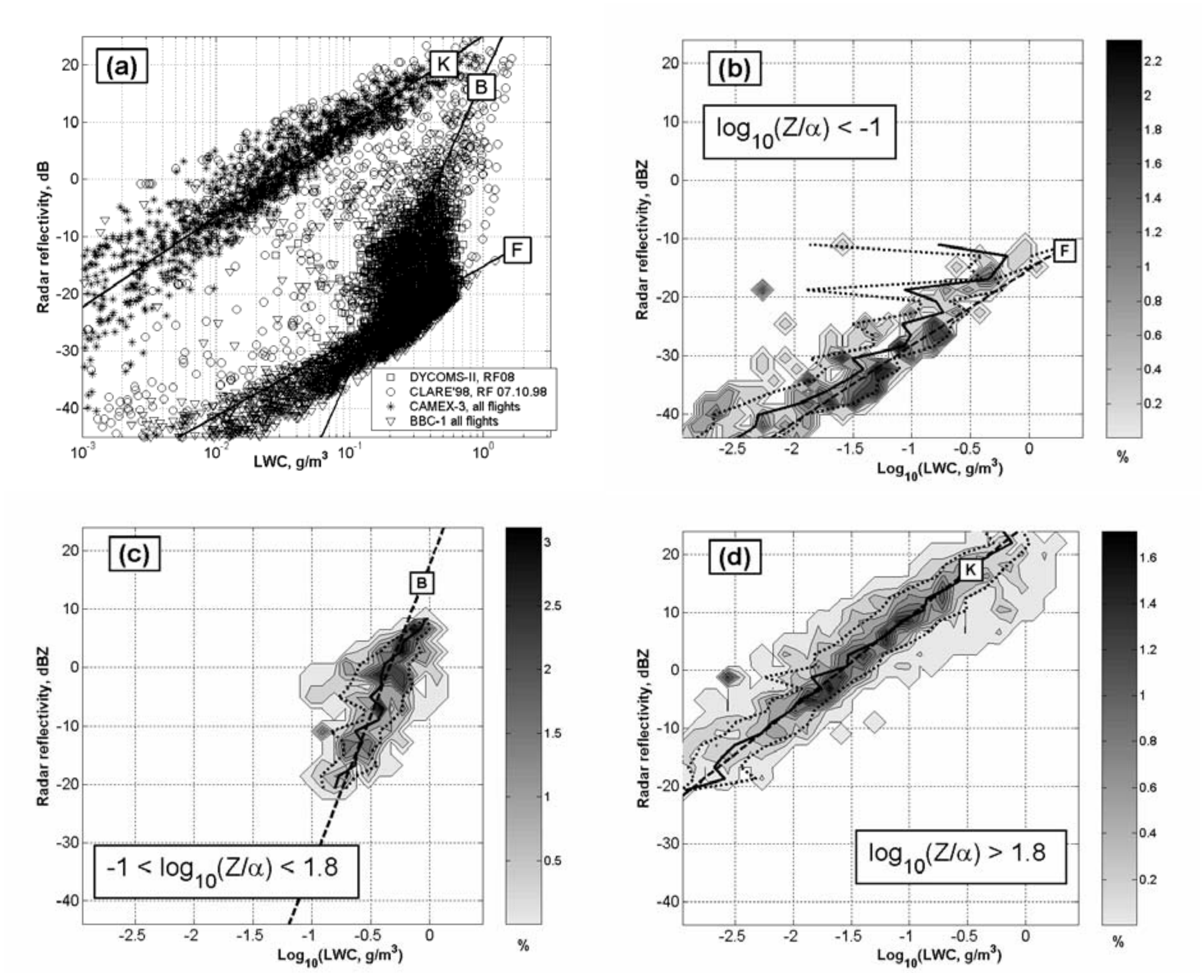

Fig. 2: Two-dimensional diagrams of the *Z*-LWC relation derived from in-situ aircraft data from four different field campaigns (see also Tab. 2); (a) – all analysed datasets, (b) – for the cloud "without drizzle" (F), (c) – for the cloud "light drizzle" (B), and (d) – for the cloud "heavy drizzle" (K). The categorization has been carried using the radar reflectivity to lidar optical extinction ratio: (b) $\log_{10}(Z/\alpha)$ < -1; (c) -1 < $\log_{10}(Z/\alpha)$< 1.8; and (d) $\log_{10}(Z/\alpha)$> 1.8 (according to K06). In (b)-(d) the dashed line represents the derived *Z*-LWC relationship, the bold line the average *Z* value for a given LWC and the dotted line the corresponding standard deviation.

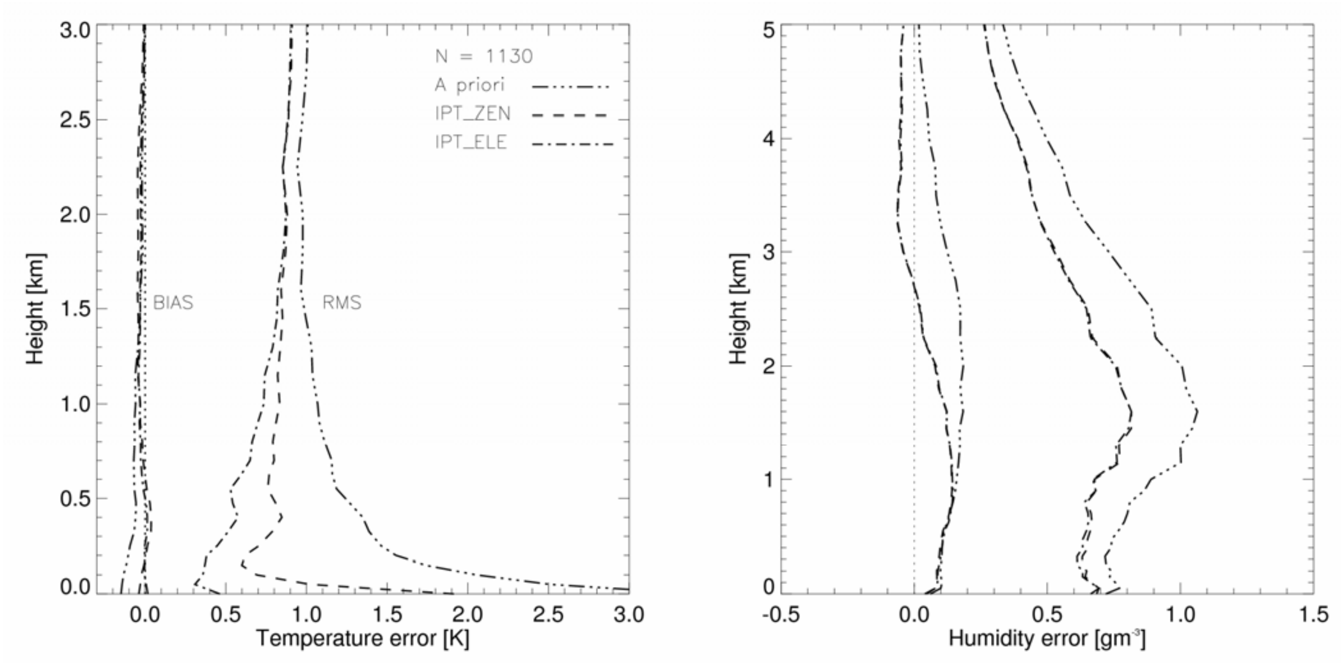

Fig. 3: Temperature (3a, left) and humidity (3b, right) BIAS and RMS errors for IPT application to simulated radiances from 1130 clear-sky radiances. The dashed (IPT_ZEN) and dashed-dotted (IPT_ELE) show the results using only zenith TB observations, respectively zenith and elevation scanning observations. Additionally shown are the errors of the a priori profile, which states the linear interpolation between two 12-hourly radiosondes. Note that in the humidity plot IPT_ZEN and IPT_ELE cannot be differentiated because they show nearly the same values.

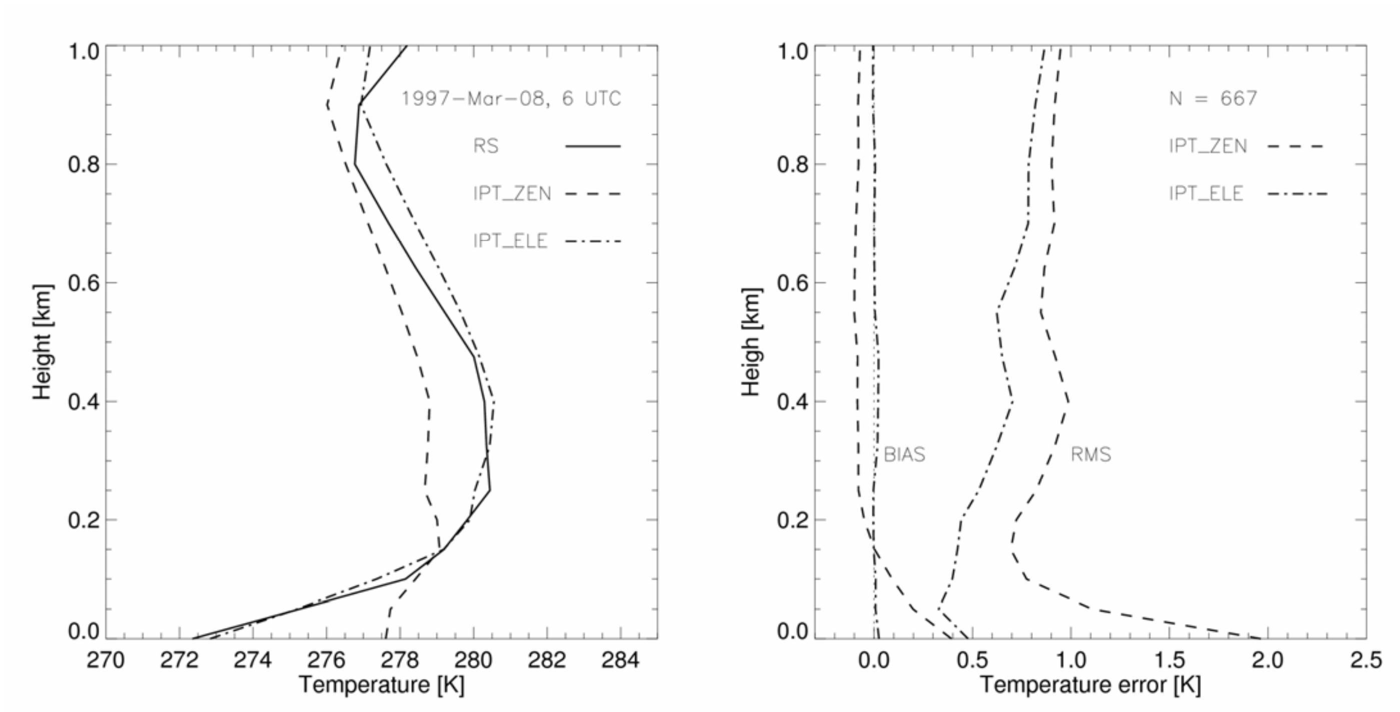

Fig. 4: (a, left): Performance of IPT_ELE and IPT_ZEN in a strong low-level inversion case compared to the radiosonde (RS). (b, right): BIAS and RMS errors of IPT_ZEN and IPT_ELE applied to all the simulated data (Fig. 3) showing boundary layer inversion.

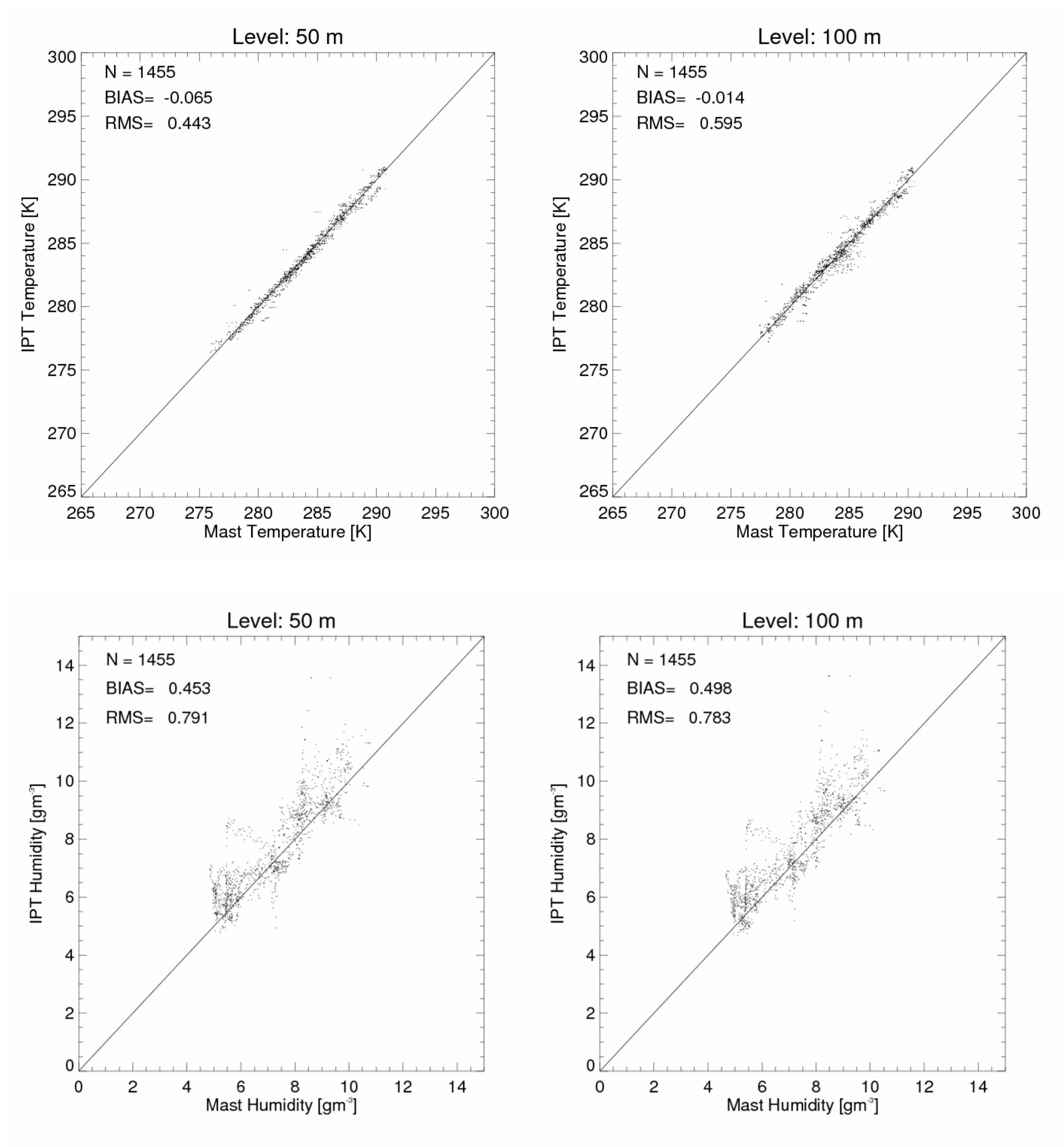

Fig. 5: Comparisons of IPT and mast measurements of temperature (top) and humidity (bottom) at levels 50 and 100 m above ground.

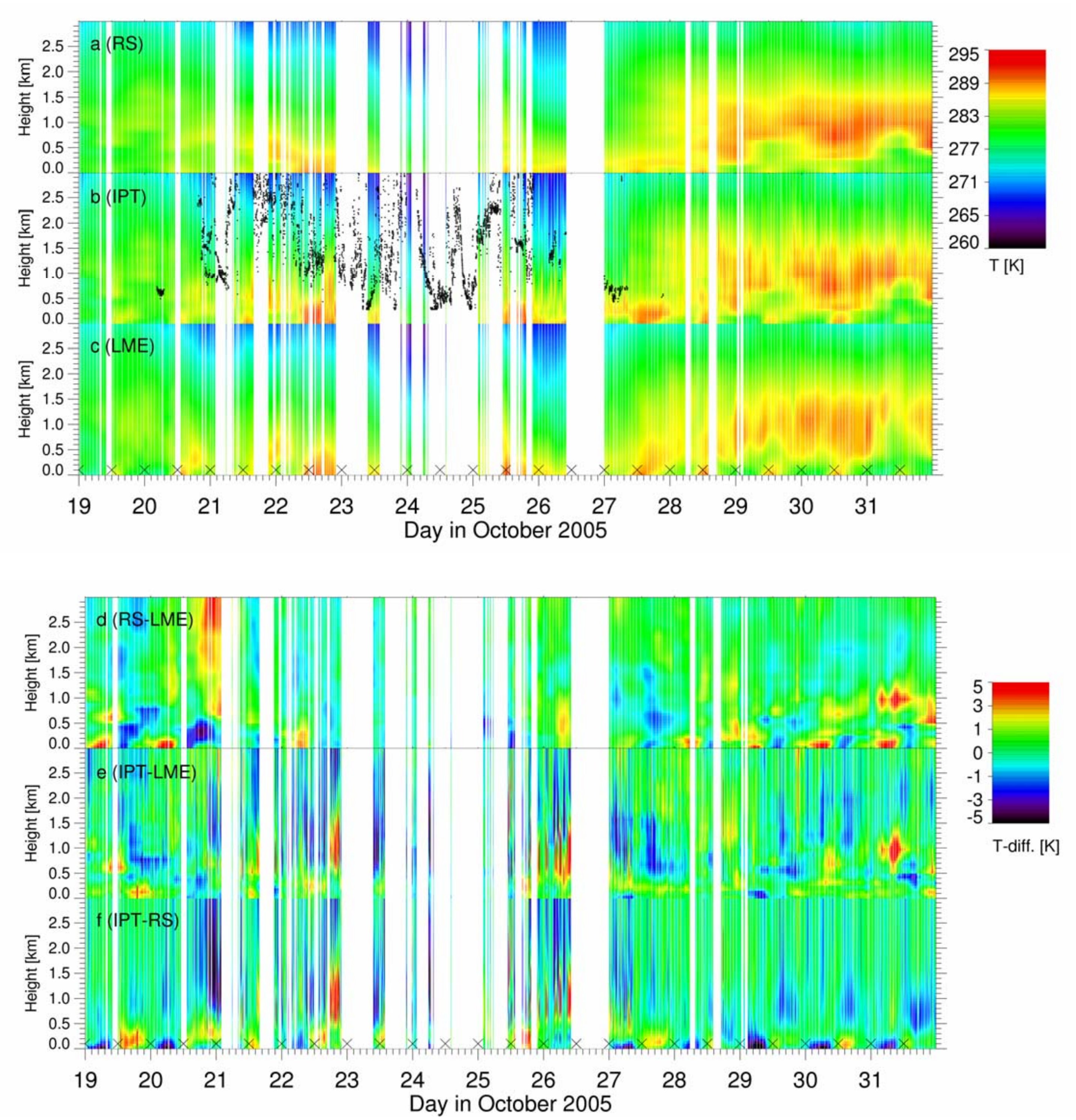

Fig. 6: Time series of temperature and cloud base (black dots) in the lowest 3 km between 19 October 2005 and 31 October 2005. (a): interpolated radiosonde profiles (12 hourly), (b): retrieved IPT profiles, (c): LME model profiles. Also: Time series of temperature difference (d): interpolated radiosonde – LME profiles (e): IPT – LME profiles, (f): IPT – interpolated radiosonde profiles. Radiosonde ascent times are marked "x". The vertical white bands denote times when the IPT could not be applied, mostly due to missing data of one of the instruments, precipitation, not fulfilled convergence criteria or radiometer calibration.

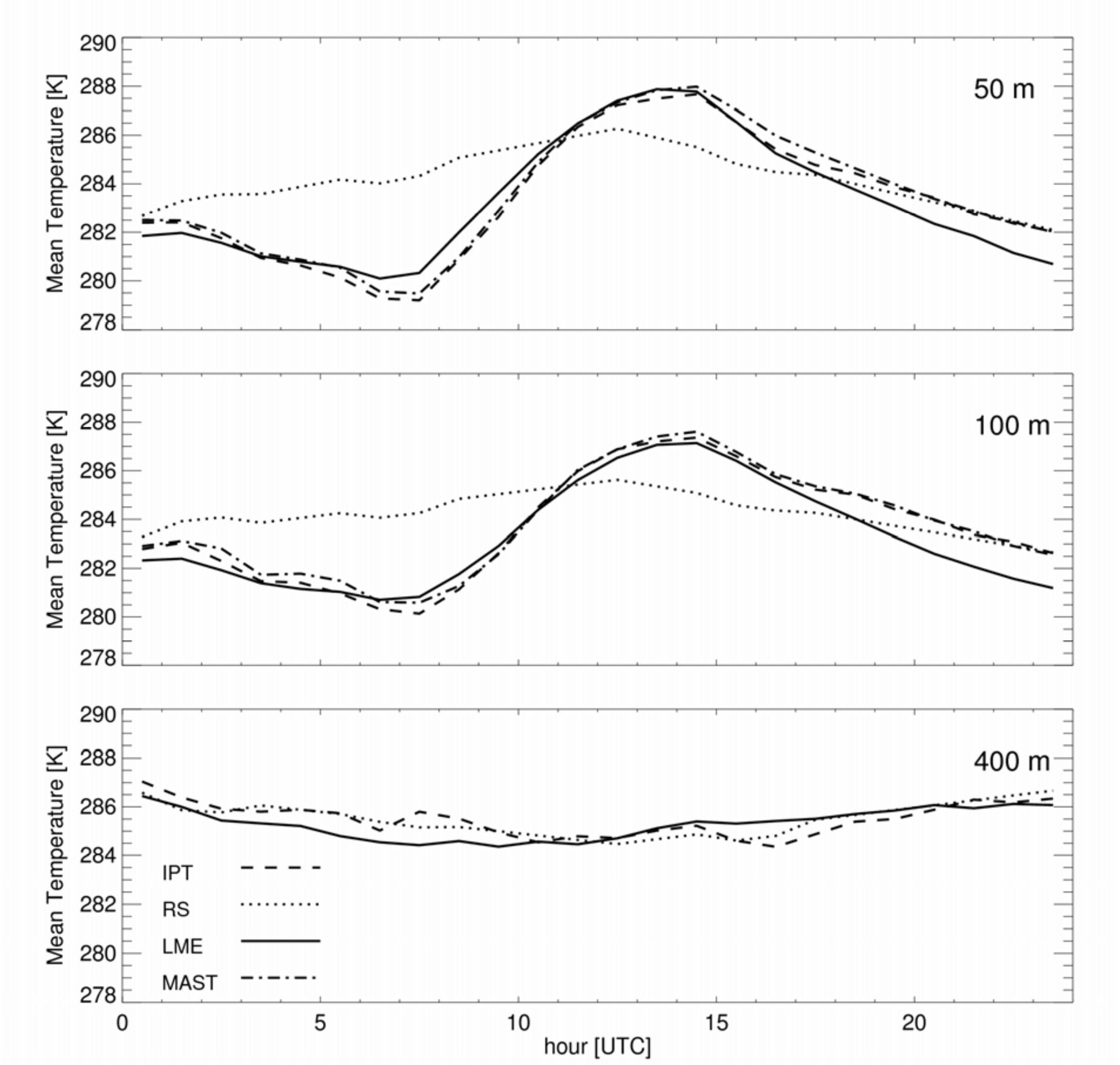

Fig. 7: Mean diurnal cycle of temperature derived during the 5 practically cloud-free days 27-31 October 2005 during LAUNCH for the different measurement-types IPT, radiosonde (RS) and mast in comparison to the 24-h LME forecasts initialized at 0000 UTC. Results at 400 m do not include any mast measurements

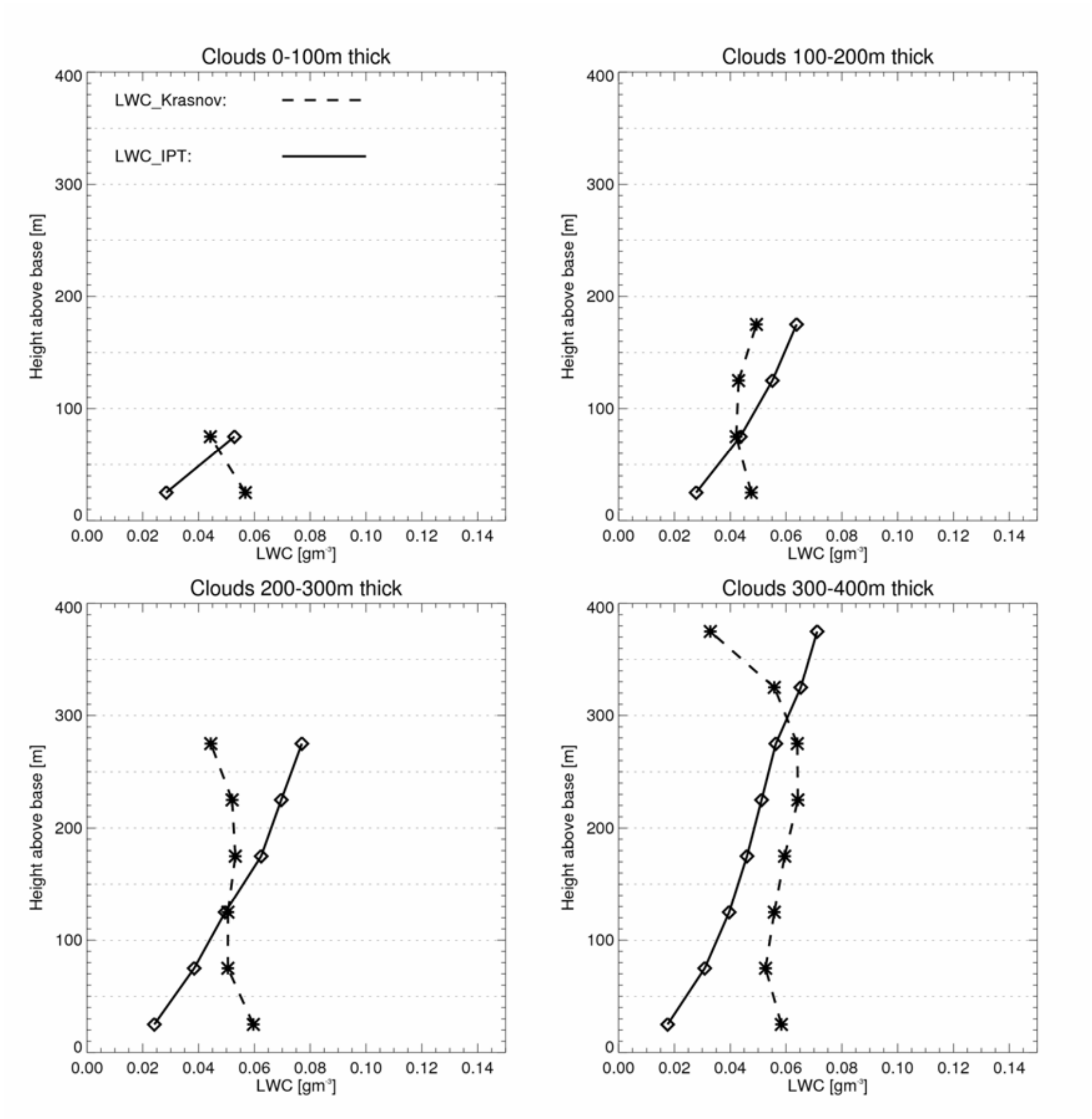

Fig. 8: Mean derived profiles of LWC from IPT and K06 during 13 days of the LAUNCH 2005 campaign. In order to be able to compare the results, clouds were binned into 4 categories of vertical extension (0-100m, 100-200m, 200-300m and 300-400m).

Tab. 1: Critical cloud base height in m for boundary layer profiling. Cloud bases higher than the critical cloud base have an influence of less than 0.1 K on TB(θ, ν). The abbreviation "**n.i.**" (= no influence) indicates that no clouds were detected that had an influence of more the 0.1 K on TB(θ, ν).

	ν=54.94 GHz	ν=56.66 GHz	ν=57.3 GHz	ν=58.0 GHz
θ=90°	**4553**	**282**	**69**	**n.i.**
θ=42°	**2328**	**0**	**n.i.**	**n.i.**
θ=30°	**1071**	**n.i.**	**n.i.**	**n.i.**
θ=19.2°	**320**	**n.i.**	**n.i.**	**n.i.**
θ=10.2°	**0**	**n.i.**	**n.i.**	**n.i.**
θ=5.4°	**n.i.**	**n.i.**	**n.i.**	**n.i.**

Tab. 2: *a*, *b* parameters used for the different cloud types (Z-LWC relationships, $Z = a\mathrm{LWC}^b$).

Cloud type	**Notation in Fig. 2**	*a*	*b*	**Reference**
Cloud "without drizzle"	**F**	0.012	1.16	Fox and Illingworth (1997)
Cloud with "light drizzle"	**B**	57.54	5.17	Baedi et al. (2000)
Cloud with "heavy drizzle"	**K**	323.59	1.58	Krasnov and Russchenberg (2002)